CHEMISTRY OF MATERIALS

Article

pubs.acs.org/cm

Fe (Oxy)hydroxide Oxygen Evolution Reaction Electrocatalysis: Intrinsic Activity and the Roles of Electrical Conductivity, Substrate, and Dissolution

Shihui Zou,[†,‡] Michaela S. Burke,[‡] Matthew G. Kast,[‡] Jie Fan,[†] Nemanja Danilovic,[§] and Shannon W. Boettcher*[,‡]

[†]Key Lab of Applied Chemistry of Zhejiang Province, Department of Chemistry, Zhejiang University, Hangzhou, 310027, China

[‡]Department of Chemistry and Biochemistry, University of Oregon, Eugene, Oregon 97403, United States

[§]Proton OnSite, Wallingford, Connecticut 06492, United States

Supporting Information

ABSTRACT: Fe cations dramatically enhance oxygen evolution reaction (OER) activity when incorporated substitutionally into Ni or Co (oxy)hydroxides, serving as possible OER active sites. Pure Fe (oxy)hydroxides, however, are typically thought to be poor OER catalysts and are not well-understood. Here, we report a systematic investigation of Fe (oxy)hydroxide OER catalysis in alkaline media. At low overpotentials of ∼350 mV, the catalyst dissolution rate is low, the activity is dramatically enhanced by an AuO_x/Au substrate, and the geometric OER current density is largely independent of mass loading. At higher overpotentials of ∼450 mV, the dissolution rate is high, the activity is largely independent of substrate choice, and the geometric current density depends linearly on loading. These observations, along with previously reported in situ conductivity measurements, suggest a new model for OER catalysis on Fe (oxy)hydroxide. At low overpotentials, only the first monolayer of the electrolyte-permeable Fe (oxy)hydroxide, which is in direct contact with the conductive support, is OER-active due to electrical conductivity limitations. On Au substrates, Fe cations interact with AuO_x after redox cycling, leading to enhanced intrinsic activity over FeOOH on Pt substrates. At higher overpotentials, the conductivity of Fe (oxy)hydroxide increases, leading to a larger fraction of the electrolyte-permeable catalyst film participating in catalysis. Comparing the apparent activity of the putative Fe active sites in/on different hosts/surfaces supports a possible connection between OER activity and local structure.

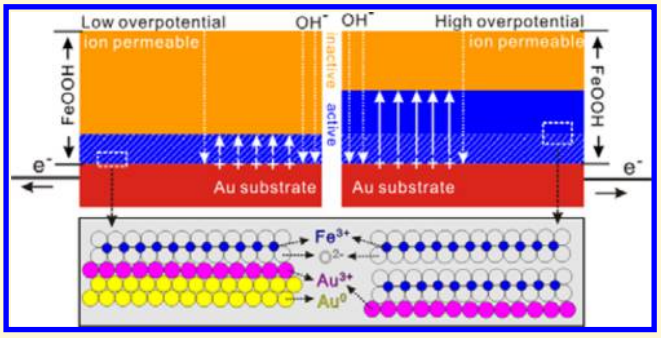

1. INTRODUCTION

The oxygen evolution reaction (OER) has slow kinetics (i.e., high overpotential) and limits the efficiency of a number of clean energy technologies including rechargeable metal-air batteries, water-electrolysis systems, and solar-fuels devices.[1−5] In order to develop active, stable, and inexpensive oxygen-evolution catalysts (OECs), there has been a large number of studies on first-row transition metal oxides and (oxy)-hydroxides, especially of Ni, Co, Fe, and Mn, under neutral to basic conditions.[6−13] Nevertheless, due to complexity in the possible surface phases, incidental impurity incorporation, and complicating effects of electronic conductivity and electrochemically active surface area, the active sites and fundamental correlations of activity to composition and structure remain unclear.[14−16]

Due to high crustal abundance and nontoxicity, Fe-based OECs are appealing.[13,17] Generally, however, iron-based OECs have been considered to have low OER activity.[18−21] The volcano curve described by Trasatti[19] correlated the activity with the enthalpy of a lower to higher oxide transition and indicated that the activity of iron oxide was much lower than that of cobalt and nickel oxide. A similar conclusion was drawn by Subbaraman et al. Using the oxophilicity of the metal cation (i.e., the M−OH bond strength) as a descriptor, they concluded that the OER activity of 3d metal (oxy)hydroxides followed the order Ni > Co > Fe > Mn.[21]

On the other hand, Fe is particularly well-known for its incorporation as a dopant/impurity into Ni/Co-based OECs.[14,15,22−32] Corrigan[22] first showed that Fe impurities introduced from the electrolyte or coprecipitated into thin-film Ni (oxy)hydroxide dramatically lower the OER overpotential. Recently, we showed that the incidental incorporation of Fe impurities from electrolytes was responsible for the high catalytic performance of Ni oxides and (oxy)hydroxides, whereas rigorously Fe-free Ni catalysts are intrinsically poor OECs.[14,15] Friebel et al. identified the local structures and site-

Received: September 1, 2015
Revised: November 11, 2015
Published: November 11, 2015

DOI: 10.1021/acs.chemmater.5b03404
Chem. Mater. 2015, 27, 8011−8020

specific overpotentials of Ni and Fe cations in Ni−Fe (oxy)hydroxide using operando X-ray absorption spectroscopy (XAS) and density functional theory calculations, respectively.[26] The unusually short Fe−O bond distances of the octahedral Fe^{3+} site and the more optimal adsorption energies of proposed OER intermediates led to the conclusion that Fe was the active site. We further found that Fe enhanced the OER activity of Co (oxy)hydroxide ~100-fold.[32] By studying the electrical conductivity and stability in situ, we also hypothesized that Fe was the active site and that the Ni or Co (oxy)hydroxide primarily provided an electrically conductive, chemically stabilizing, and high surface area host. The low apparent activity for FeOOH itself was associated with low electrical conductivity. Lyons and co-workers published a series of papers on electrochemically conditioned Fe metal electrodes and proposed a mechanism involving the active participation of iron oxyhydroxide surfaquo groups.[11,20,33−36] They studied the Tafel behavior and argued that the rate-determining step of the OER depended strongly on the conditions (e.g., potential, OH^- ion concentration) under which the iron oxyhydroxide film is generated.

We further benchmarked the OER activity of (oxy)-hydroxides in the absence of confounding surface area, conductivity, and Fe impurity affects and found a new activity trend of $Ni(Fe)O_xH_y$ > $Co(Fe)O_xH_y$ > FeO_xH_y > CoO_xH_y > NiO_xH_y > MnO_xH_y (where the oxyhydroxides are indicated by a general formula so as not to specify a specific structure or cation oxidation state).[37] This trend is different from previous experimental and computational trends[19,21,34,38−42] and suggests Fe plays an important role in OER catalysis across multiple systems.

The observation that FeOOH is the most active among the single first-row transition metals motivates efforts to understand how it operates. Fundamental studies, however, are limited by a number of factors.[32,37,43] (1) FeOOH is chemically unstable to dissolution in alkaline media, and the relationship between instability and activity are not well-understood.[32,37,43] (2) Because Fe does not exhibit clear reversible redox waves in the experimentally accessible electrochemical window, it is not possible to accurately measure the number of electrochemically active sites by integrating redox waves.[32] (3) The poor electrical conductivity of FeOOH slows electron transfer between the underlying conductive substrate and active sites within the film, convoluting activity data.[32,37,44,45] In sum, these challenges have limited our basic understanding of intrinsic activities in Fe-based OER catalysts.

Here, we report a systematic study of FeOOH OER catalysts in alkaline media with the aim of addressing each of the above issues. First, we prepared films by three different deposition methods and found evidence that FeOOH is the surface species responsible for OER. Using a quartz crystal microbalance (QCM) to monitor mass in situ, we found that FeOOH dissolves in 1 M KOH electrolyte and that the dissolution rate increases with overpotential. Measuring FeOOH films with different thicknesses (mass loading) revealed that the geometric OER current density is constant with loading at low overpotentials, whereas it increases with loading at high overpotentials. These observations, coupled with our earlier in situ conductivity measurements, led us to propose a model in which only a fraction of the FeOOH film next to the conducting substrate is electron-accessible and OER-active. At more anodic potentials, the electrical conductivity increases, along with the fraction of the film that is OER-active. Finally, we report the OER activity enhancement of FeOOH on Au substrates, which appears to be dependent on the formation of mixed FeOOH-AuO_x film upon potential cycling across the Au redox wave in the presence of solution Fe impurities or a FeO_x film. In sum, these results improve our fundamental understanding of the factors governing the apparent OER activity of Fe-based catalysts and the role of Fe in activating other catalyst systems.

2. EXPERIMENTAL SECTION

2.1. Film Preparation. Fe (oxy)hydroxide, oxide, and metal films were deposited onto Au/Ti or Pt/Ti coated 5 MHz quartz crystal microbalance (QCM) crystals by electrodeposition, spin-casting, and thermal evaporation, respectively. The QCM crystals were 1 in. in diameter with an active electrode area of 1.38 cm^2 and were obtained from Stanford Research Systems. Prior to spin-casting and thermal evaporation, the QCM crystals were cleaned by ultrasonication in a 6.25% (v/v) solution of Contrad-70 detergent (Decon Laboratories) in 18.2 MΩ cm water at 60 °C for 30 min, rinsed with 18.2 MΩ cm water, and then cleaned with oxygen plasma for 15 min.

2.1.1. Electrodeposition. Fe (oxy)hydroxide was cathodically deposited from unstirred solution of 0.1 M $FeCl_2{\cdot}4H_2O$ (Alfa-Aesar, 98% trace metals basis) and 0.05 M $NaNO_3$ (Mallinckrodt Chemicals, >98%) in 18.2 MΩ cm H_2O. A two-electrode cell was used with carbon-cloth (Fuel Cell Earth) as a counter electrode. To prevent the oxidation of $FeCl_2$ into insoluble FeOOH, the solution was covered in Parafilm and purged with N_2 for ~20 min prior to $FeCl_2$ addition and between depositions. Depositions at −0.2 mA cm^{-2} ranging from 15 to 240 s produced films with masses between 0.8 and 30 $\mu g\ cm^{-2}$. The film mass was determined from the difference between the measured QCM resonance frequency in 18.2 MΩ cm H_2O before and after deposition. Prior to deposition, all QCM crystals were cleaned in 1 M H_2SO_4(aq) (Sigma-Aldrich) via potential cycling (2 cycles, 2.5 to −2.5 V at 200 mV s^{-1}) and then checked in 1 M KOH solution (2 CV cycles, 0 to 0.7 V vs Hg/HgO at 10 mV s^{-1}) to ensure complete film stripping. For $Co_{0.54}Fe_{0.46}OOH$ and $Ni_{0.75}Fe_{0.25}OOH$ films, the total metal content in the deposition solution was held at 0.1 M, and 0.06 M 99.999% $Co(NO_3)_2{\cdot}6H_2O$ or 0.09 M $Ni(NO_3)_2{\cdot}6H_2O$ was added. Typical deposition for $Ni_{0.75}Fe_{0.25}OOH$ and $Co_{0.54}Fe_{0.46}OOH$ was accomplished by applying −0.1 and −2 mA cm^{-2} (cathodic), respectively. Fe content was measured by X-ray photoelectron spectroscopy (XPS). Further experimental detail has been published elsewhere for these standard methods.[15,32]

2.1.2. Spin-Casting. Fe oxide films (~2 nm) were deposited from a precursor solution via spin-casting. As described previously,[14] the precursor solution was freshly prepared by dissolving $Fe(NO_3)_3{\cdot}9H_2O$ (>99.9%, Sigma-Aldrich) in ethanol at a concentration of 0.05 M. Triton X-100 (J.T. Baker) was added to give 0.15 g of Triton per mmol of Fe^{3+}. The precursor solution was spun onto cleaned QCM crystals at 5000 rpm for 90 s and then annealed in air on a hot plate at 300 or 200 °C for ~5 min, as specified in the text. Spin-cast Fe oxide films for diffraction measurements were spun from 1.0 M $Fe(NO_3)_3{\cdot}9H_2O$ in 50:50 ethanol/H_2O with 0.05 g mL^{-1} Triton X and annealed for 10 min at 300 °C to provide a thicker film and thus better diffracted intensity.

2.1.3. Thermal Evaporation. Fe metal films (~100 nm) were deposited at 5 Å s^{-1} onto previously cleaned QCM substrates by thermal evaporation from Fe pieces (Alfa-Aesar, 99.9%) in an Angstrom Engineering Åmod deposition system at a base pressure $<4 \times 10^{-6}$ Torr.

2.2. Characterization. The film masses were calculated using the Sauerbrey equation[46] $\Delta f = -C_f \times \Delta m$, where Δf is the experimental frequency change (Hz), C_f is the sensitivity factor of the 5 MHz AT-cut quartz crystal (~64.5 Hz $\mu g^{-1}\ cm^2$),[32] and Δm is the change in mass per unit area ($\mu g\ cm^{-2}$). Grazing incidence X-ray diffraction (GIXRD) patterns were collected on a Rigaku SmartLab diffractometer (Cu Kα X-ray, incident angle of 0.4°, 0.1° step size, and 72 s per step integration) with parallel beam optics, diffracted-beam monochromator (to remove Fe fluorescence), knife edge, and K-β

DOI: 10.1021/acs.chemmater.5b03404
Chem. Mater. 2015, 27, 8011−8020

filter. Scanning electron microscope (SEM) images were recorded on a Zeiss Ultra 55 SEM operating at 5 keV. X-ray photoelectron spectra (XPS) and angle resolved XPS (ARXPS)[47] were collected using an ESCALAB 250 (Thermo Scientific) with an Al Kα monochromatic source (150 W, 20 eV pass energy, and 500 μm spot size). A Mg Kα (450 W, 75 eV pass energy) nonmonochromatic flood source was used to determine the compositional information (Ni/Fe and Co/Fe). All binding energies were referenced to the Au 4f peaks (84.0 eV) when on Au substrates and C 1s (284.5 eV) on metallic Fe (adventitious surface carbon), charge neutralized using an in-lens electron source, and grounded using copper tape.

2.3. Electrochemical Measurements. All electrochemical measurements were performed in a three-electrode poly(tetrafluoroethylene) (PTFE) or poly(methylpentene) (PMP) cell with an Hg/HgO reference electrode (CH Instruments), Pt wire (contained in a coarse plastic fritted compartment) as a counter electrode, and Au/Ti or Pt/Ti-coated quartz crystals coated with the Fe-based film as a working electrode. Measurements were made at ambient temperature with a BioLogic (SP300 or SP200) potentiostat in 1 M KOH electrolyte (semiconductor grade, 99.99%, Sigma-Aldrich). Prior to use, all plastic components were cleaned with 1 M H_2SO_4. Pt counter electrodes were periodically cleaned by dipping in aqua regia for ~20 s, followed by a 18.2 MΩ cm H_2O rinse. Ultra high-purity O_2 gas was bubbled through the electrolyte for at least 20 min prior to electrochemical measurements. Magnetic stirring was used to eliminate bubble accumulation.

Unless otherwise specified, all values of current density were normalized with respect to the geometric surface area of the QCM crystal (1.38 cm^2). Cyclic voltammetry (CV) and steady-state Tafel measurements were corrected for uncompensated series resistance (R_u). R_u was determined by equating R_u to the minimum impedance between 1 kHz and 1 MHz, where the phase angle was closest to zero. Typically, R_u was ~2−6 Ω for Au/Ti QCM electrodes and ~4−15 Ω for Pt/Ti QCM electrodes. The overpotential (η) was calculated using the equation $\eta = E_{measured} - E_{rev} - iR_u$. $E_{measured}$ is the recorded potential vs Hg/HgO, and E_{rev} is the reversible potential (0.30 V vs Hg/HgO at pH 14, calibrated against RHE) for the OER. For chronoamperometry (CA) measurements, the ohmic drop was compensated at 100% using a manual iR_u compensation method (BioLogic EC-lab).

3. RESULTS AND DISCUSSION

3.1. Film Preparation and Structural Characterization. A number of methods have been used to prepare Fe-based materials for OER, including electrodeposition,[13,48,49] thermal decomposition,[14] photodeposition,[50−52] and potential cycling of Fe metal.[11,20] Although films prepared by different methods have different crystal structures and morphologies, the active surface layers formed under OER conditions are likely composed of iron oxyhydroxide, as predicted by equilibrium Pourbaix diagrams[53] and as has been observed in several cases.[49,52] We prepared films by different deposition methods (electrodepostion, spin-casting, and thermal evaporation) to investigate the relationship between the starting materials and surface structures found under OER-relevant conditions.

GIXRD patterns in Figure 1A show the bulk structural information on as-deposited films. The diffraction pattern for the electrodeposited film has seven broad peaks at 11.8°, 16.8°, 26.7°, 35.2°, 39.2°, 46.4° and 55.9°, corresponding to (100), (200), (310), (211), (301), (411), and (521) of β-FeOOH (ICSD 31136), respectively. Other oxyhydroxide phases (e.g., α, δ, γ) may form under other deposition conditions.[32,54] No strong diffraction peaks belonging to Fe species are detected for the spin-cast film, probably due to a largely amorphous structure from the low annealing temperature (see Figure S1 for expanded view of the weak, broad diffracted intensity that is present). For the evaporated film, the sharp peaks at 44.7° and 65.0° are indexed to (110) and (200) of Fe metal (ICSD 52258). The observation that the as-deposited films have different bulk phases is expected based on the different deposition methods used in each case. The electrodeposition proceeds via the cathodic reduction of NO_3^- at the electrode surface, which increases the pH to drive iron hydroxide precipitation and form a film, as predicted by the Pourbaix diagram.[13,48,49] The spin-cast film is formed via the thermal decomposition in air of iron nitrate into amorphous/nanocrystalline iron oxides. The metallic films are formed from thermal evaporation of Fe metal under high vacuum with only the surface accessible for oxidation to oxyhydroxide (i.e., rust).

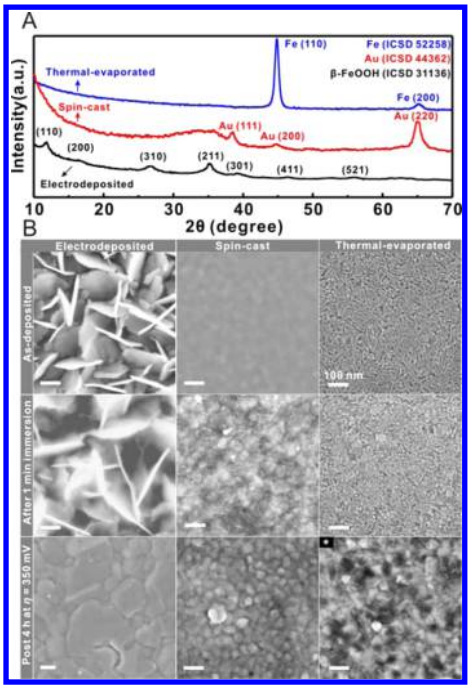

Figure 1. (A) GIXRD of as-deposited films. (B) SEM images of samples as-deposited (top), after 1 min immersion in 1 M KOH at room temperature (middle), and after 4 h anodic polarization at η = 350 mV in 1 M KOH, except for Fe metal films, which were polarized for 12 h (bottom). The scale bars are 100 nm. Spin-cast films were annealed at for 5 min 200 °C for SEM images and 10 min at 300 °C for the thicker ones used for diffraction measurements.

The different deposition methods also result in different surface morphologies (Figure 1B). The electrodeposited FeOOH film has a porous platelet-like structure, which is in good agreement with the morphology expected for first-row transition metal (oxy)hydroxides.[11,55−57] The evaporated Fe metal film consists of grains roughly 9 nm in diameter and 40 nm in length. No obvious surface texture was found for spin-cast films. After being immersed in 1 M KOH electrolyte for 1 min at room temperature, the film morphology evolves. The spin-cast film roughens, likely as the surface amorphous iron oxides convert into Fe (oxy)hydroxide. The increased XPS O 1s signal at ~531.7 eV on the spin-cast film after immersion in KOH (Figures S2 and S3) further indicates the formation of surface hydroxides and thus FeOOH. The surface morphology of the Fe metal film changes only slightly after exposure to KOH at room temperature. XPS results (Figure S4), however, show that the majority of near-surface species after 5 s polarization at η = 350 mV are oxidized forms of Fe, e.g., FeOOH. If the Fe metal film is oxidized at 200 °C in air for 1 h and then immersed in 1 M KOH, then a similar roughened

DOI: 10.1021/acs.chemmater.5b03404
Chem. Mater. 2015, 27, 8011−8020

morphology was found (Figure S4). These simple studies suggest that, independent of film preparation pathway, Fe (oxy)hydroxide forms the surface species under rest conditions in basic media and is thus the phase that is most relevant for OER catalysis on these films. With this in mind, the remainder of the study was completed on the electrodeposited FeOOH films. We also note that, although we refer to the catalyst as FeOOH, the chemical composition under OER conditions may change and a more general description would be FeO_xH_y.

3.2. Stability and Activity of FeOOH at Different Overpotentials. Stability is required for electrocatalysts.[19,32,58−60] Frydendal et al. reported a protocol to access the stability of OECs by combining inductively coupled plasma mass spectrometry (ICP-MS) with QCM measurements.[59] Danilovic et al. compared the OER activity and chemical stability of five different noble metal oxides in acid and found that the most active metals were those with the least chemical stability (i.e., high solubility in acid).[60] We previously reported that FeOOH is unstable and dissolves under OER conditions, whereas Co(Fe)OOH and Ni(Fe)OOH do not.[32]

To further assess the stability of FeOOH, chronoamperometry experiments were performed at different overpotentials on both Au and Pt QCM crystals. Dramatic mass loss is detected during anodic polarization on both Au and Pt, indicating that FeOOH is soluble in 1 M KOH(aq) during the OER (Figure 2A and Table 1). SEM images shown in Figure 1B confirm that after 4 h polarization at η = 350 mV the film is almost entirely dissolved. The inset in Figure 2B shows that the dissolution rate depends on potential. We speculate that the higher dissolution rates at more anodic potentials are due to the faster conversion of FeOOH into soluble FeO_4^{2-}, as suggested by

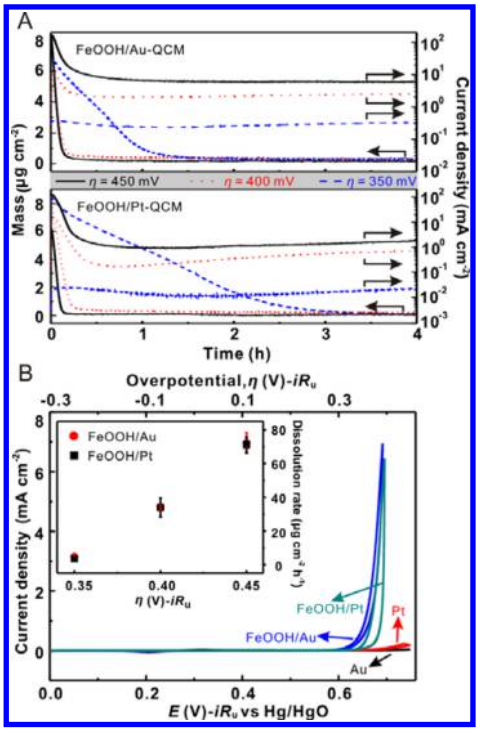

Figure 2. (A) Chronoamperometry measurements on FeOOH on Au (top) and Pt (bottom) at different overpotentials. (B) Voltammetry of Au, Pt, FeOOH/Au, and FeOOH/Pt at 10 mV s^{-1} in 1 M KOH. The inset shows the dissolution rates calculated from the initial linear region of the mass−time curves in panel A.

Table 1. Dissolution Rate and Residual Mass after 4 h Polarization on FeOOH/Au and FeOOH/Pt[a]

measurement	η (mV)	FeOOH/Au	FeOOH/Pt
dissolution rate (μg cm^{-2} h^{-1})	350	5 ± 1	4 ± 1
	400	34 ± 1	34 ± 5
	450	72 ± 6	71 ± 5
residual mass after 4 h polarization (μg cm^{-2})	350	0.1 ± 0.2	0.1 ± 0.1
	400	0.2 ± 0.1	0.1 ± 0.2
	450	0.1 ± 0.1	0.2 ± 0.1
initial active mass (μg cm^{-2})	350	0.1 ± 0.2	0.1 ± 0.1
	400	0.9 ± 0.5	1.5 ± 3
	450	3 ± 3	8 ± 4

[a]All values are the average from three independent experiments.

equilibrium Pourbaix diagrams.[53] Interestingly, even after polarizing at η = 450 mV for 4 h, a small amount of FeOOH (ca. 0.1 μg cm^{-2}) seems to remain on the substrates, suggesting a possible chemical interaction that will be discussed below. This is further confirmed by angle-resolved XP spectra (Figure S5), which shows that a thin layer FeOOH remains after 1 h polarization at η = 350 mV. We note the uncertainty in these residual mass measurements is high due to limitations of the QCM measurement but that the error sets an upper limit on the residual mass, and we are certain that some FeOOH remains from the XPS results.

Figure 2A shows geometric current density (right axis) and mass (left axis) as a function of time at different overpotentials. At η = 350 mV, the OER current after 4 h polarization (ca. 0.33 mA cm^{-2}) is comparable to the initial current density (ca. 0.37 mA cm^{-2}), even though >95% of the mass is lost. In contrast, at η = 400 mV, the current density after 4 h polarization (ca. 2.5 mA cm^{-2}) is only 22% of the initial current density (ca. 11.5 mA cm^{-2}), whereas at η = 450 mV, the current density decreases by 96% after 4 h polarization. Assuming that all residual FeOOH species are active and that the current density is completely determined by the FeOOH film (i.e., no substrate enhancement), we can estimate the initial amount of OER-active FeOOH by dividing the residiual mass by the fractional change in the current relative to the initial film (Table 1). We note that the errors are larger than the values in some cases due to the larger error in estimating the residual mass (due to the detection limit of the QCM). However, our measurements systematically show an average residual mass greater than zero. It is also evident that some FeOOH must remain on the surface because the OER activity remains much larger than the bare Au or Pt substrate and we observe clear Fe 2p peaks by XPS (Figure S5). The estimates of the film active fraction are further consistent with those obtained by considering the electrical conductivity measured in situ, as discussed below.

We also observe that, for a similar amount of FeOOH, the current density of FeOOH/Au is higher than that of FeOOH/Pt at η = 350 mV, whereas at η = 450 mV, the current density of FeOOH/Au and FeOOH/Pt is similar. These results imply that the OER activity of FeOOH is more influenced by the substrate at low overpotentials than at high overpotentials. Assuming that all of the Fe cations remaining in the film are active, the effective mass-based total metal turnover frequencies (TOF_{tm}) at η = 350 mV are 0.25 and 0.07 s^{-1} on Au and Pt substrates, respectively, which is much higher than that of Fe-free CoOOH/Au (0.01 s^{-1}) and Fe-free NiOOH/Au (0.003 s^{-1}).[37] These TOF_{tm} values, defined as O_2 generated per second per metal cation, are calculated using the entire

DOI: 10.1021/acs.chemmater.5b03404
Chem. Mater. 2015, 27, 8011−8020

(remaining) film mass to find the total number of transition metal cations.

3.3. Tafel Electrokinetic Analysis. Figure 3 shows steady-state Tafel plots of FeOOH/Au and FeOOH/Pt. The Tafel

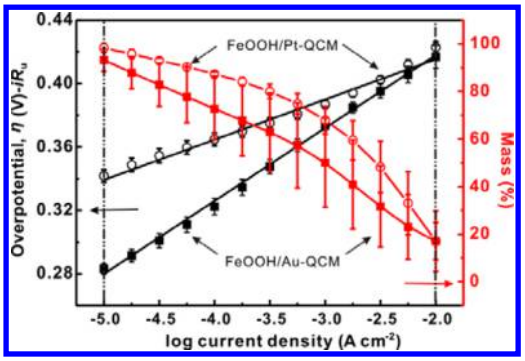

Figure 3. Steady-state Tafel measurements and in situ mass measurements on FeOOH/Au (solid) and FeOOH/Pt (open), with slopes of 46.0 ± 0.7 and 31.4 ± 0.8 mV dec^{-1}, respectively. The Tafel analysis was performed at current densities between 10^{-5} and 10^{-2} A cm^{-2} in 13 steps of 3 min in duration each.

slopes of FeOOH/Au (ca. 46 mV dec^{-1}) and FeOOH/Pt (ca. 31 mV dec^{-1}) are different, suggesting that the substrate plays a role in the OER mechanism (more discussion on this can be found below).[37] Specifically, to achieve 0.01 mA cm^{-2}, a higher overpotential is required for FeOOH/Pt than FeOOH/Au, whereas for 10 mA cm^{-2}, the overpotentials are similar. We also note that roughly constant Tafel slopes are obtained for both FeOOH/Au and FeOOH/Pt even though substantial mass is lost during the course of the measurement. This is consistent with the hypothesis that only a small amount of FeOOH next to the substrate is active for OER.

3.4. Substrate and Thickness Dependence. The apparent OER activities of transition metal oxides/(oxy)-hydroxides are influenced by the substrate as well as by the catalyst thickness.[61−66] Yeo and Bell investigated CoO_x[63] and NiOOH[64] films electrodeposited onto roughened metal electrodes and discovered that the OER activity of CoO_x or NiOOH was enhanced by electronegative metals such as Au. They also found that estimated TOFs of the CoO_x/Au or NiOOH/Au electrodes decreased with film thickness. The enhanced and thickness-dependent activity was attributed to partial electron transfer from the CoO_x or NiOOH to the more electronegative Au substrate, thus making the generation of Co^{4+} or Ni^{4+} species easier. Frydendal et al., on the other hand, used DFT calculations to suggest that the enhancement of OER activity was due to the hydrogen acceptor role of Au═O.[61] We note the surface of both Au and Pt is oxidized to form a thin oxide layer under alkaline OER conditions,[53] which may affect the interface interactions.

To evaluate the impact of the substrate on FeOOH catalysis, we recorded the steady-state current with different loadings of FeOOH at two overpotentials (350 and 450 mV) on both Au and Pt QCM crystals (Figure 4). Similar measurements on bare Au and Pt electrodes are shown for comparison. Because FeOOH dissolves during the OER, the current and mass plotted in Figure 4 were the average from the second minute in each chronoamperometry experiment. At η = 350 mV, the current density of FeOOH/Au (ca. 0.5 mA cm^{-2}) is much higher than bare Au (ca. 0.004 mA cm^{-2}) and does not change with mass loading. The calculated TOF_{tm} for FeOOH/Au thus

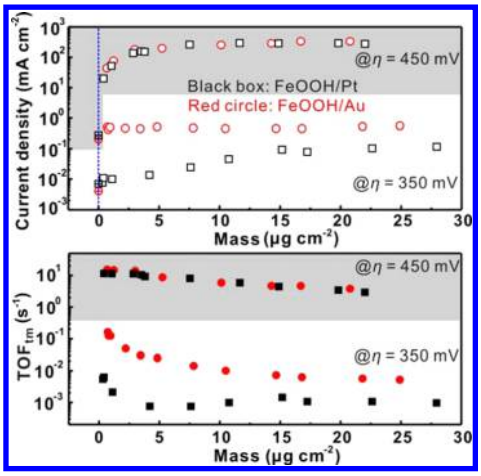

Figure 4. Steady-state current densities (top) and TOF_{tm} (bottom) for FeOOH with different mass loading on Au (red circles) and Pt (black boxes). The current densities on bare Au and Pt (mass = 0, indicated by the dotted blue line) at both potentials in Fe-free KOH are shown for reference. Because the FeOOH dissolves during OER measurements, the data shown is the average during the second minute for each film, and each point is for a different film.

decreases rapidly as the mass loading increases. The 0.7 μg cm^{-2} FeOOH/Au sample exhibits the highest TOF_{tm}, ca. 0.16 s^{-1}, which is much higher than that for the 25 μg cm^{-2} FeOOH/Au sample (ca. 0.005 s^{-1}). In the case of FeOOH/Pt, the current density at η = 350 mV first increases with the mass loading and then remains constant (this may be due to incomplete island coverage during FeOOH deposition on Pt, leading to increased interfacial FeOOH with increases in mass loading). For all loadings at η = 350 mV, the activity on Au is much larger than on Pt. The mechanism for this enhancement is discussed below.

At η = 450 mV, the current densities and TOF_{tm} of FeOOH/Au and FeOOH/Pt are similar, suggesting that the OER activity of FeOOH is no longer strongly influenced by the substrate. When the mass loading is less than 3 μg cm^{-2}, the current density is nearly proportional to the number of deposited Fe ions, resulting in a constant TOF_{tm}. With loading increasing from 3 to 7.5 μg cm^{-2}, the current density does not increase proportionally; consequently, the TOF_{tm} decreases. Once the mass loading is greater than ~7.5 μg cm^{-2}, the current density remains constant, indicating the additional mass does not contribute to the activity.

3.5. Model for the OER on FeOOH Films. Good electrical conductivity is required for heterogeneous electrocatalysts, and low electrical conductivities can make it difficult to measure intrinsic activities.[15,19,67,68] We showed that FeOOH is an insulator with measurable conductivity (~0.02 mS cm^{-1}) only at high overpotentials, >400 mV.[32] The impedance spectra (Figure S6) for FeOOH/Au with different mass loadings are nearly identical to that for bare Au, suggesting that the FeOOH films are porous with electrolyte permeated through the film to the Au electrode surface.[69] This hypothesis is further supported by the similar Au/AuO_x voltammetric peaks for the FeOOH/Au films independent of loading. If the FeOOH were not electrolyte-permeable, then increased FeOOH loading would block the Au/AuO_x surface redox processes and increase the series resistance measured by impedance.

We thus propose that only a thin electron-accessible layer of FeOOH (Figure 5) is active for OER. The thickness of this

DOI: 10.1021/acs.chemmater.5b03404
Chem. Mater. 2015, 27, 8011−8020

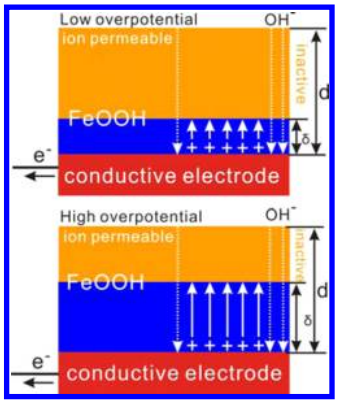

Figure 5. Schematic depicting the region of OER activity in the electrolyte-permeable FeOOH films at different overpotentials. δ is the thicknesses of electron-accessible OER-active FeOOH, and d is the thickness of the entire film.

layer (δ) depends on overpotential, as does the electrical conductivity of the film. For example, at η = 350 mV, the conductivity of FeOOH is, at most, 10^{-7} S cm^{-1} (based on the noise limit of the measurement). In order to drop <1 mV of potential across the film when passing 1 mA cm^{-2}, the film thickness must be <1 nm. If the FeOOH sheets lie flat on the substrate, then the mass of a 1 nm thick film is calculated to be ca. 0.14 μg cm^{-2} (see Supporting Information). This value is similar to that estimated from the residual film after FeOOH dissolution from QCM (0.1 ± 0.2 μg cm^{-2}). We hypothesize that for higher mass loadings the real number of active sites (i.e., that are electron-accessible) remains constant and the number of inactive sites (i.e., that are electron-inaccessible) increases. This view is consistent with the data shown for FeOOH/Au in Figure 4. For FeOOH/Pt, however, the current density did increase with loadings up to ~10 μg cm^{-2}. We propose that this is due to the lower chemical affinity of Pt for FeOOH relative to Au (which is consistent with activity enhancement observed only on Au) and thus better dispersion of the initially deposited FeOOH on Au relative to Pt. For Pt, then, the entire surface would be covered only at higher loading. We attempted to confirm this hypothesis with scanning electron microscopy, but we were unsuccessful. Further experiments, for example, using single-crystal Au and Pt with atomic force microscopy, would be helpful.

At higher overpotentials of 450 mV, the conductivity of FeOOH is 3.5 × 10^{-3} mS cm^{-1}, and to drop 1 mV potential across the film when passing 1 mA cm^{-2}, the maximum thickness (δ) is ~35 nm. If all FeOOH sheets are close-packed, then the mass of a 35 nm thick layer is ca. 5 μg cm^{-2}. Thus, when the mass loading is less than 5 μg cm^{-2} (i.e., $d < \delta$), all FeOOH sites are presumably electron-accessible and OER-active. When the mass loading is greater than 5 μg cm^{-2} (i.e., $d > \delta$), the electron-accessible (i.e., OER-active) layer thickness δ stays constant, as would the geometric current density. This hypothesis is consistent with the results in Figure 4 on both Pt and Au. The active loading of ~5 μg cm^{-2} (estimated by the simple assumptions regarding the electrical conductivity above) is similar to the experimental loading where the OER current becomes independent of loading, further supporting the model in Figure 5. We note also that at the high current densities (ca. 200 mA cm^{-2}) measured at η = 450 mV bubble or mass transport may play a role in limiting the loading dependence, although we did not observe a strong dependence of the current on the stirring rate used to dislodge bubbles (Figure S7).

Finally, the model is consistent with the differences in TOF$_{tm}$ for FeOOH on Pt and Au. At low overpotentials, only the FeOOH directly on the Au or Pt is active for OER, and it is these Fe cations that would be expected to be modulated substantially by electronic interaction with the underlying AuO$_x$ or PtO$_x$. Because the FeOOH is porous and permeated by electrolyte (as discussed above), the interfacial Fe remains active at higher loadings and the FeOOH/Au is always more active than the FeOOH/Pt. At high overpotentials, only a small portion of the active layer is strongly influenced by the substrate, and the measured activity is that largely of the bulk FeOOH. Consequently, the OER activity of FeOOH on Au and Pt is almost the same at η = 450 mV. This is consistent with the Tafel data in Figure 3, which shows that for overpotentials above ~400 mV the Tafel slopes on both Pt and Au become similar.

3.6. Comparing Matrix and Support Effects on the OER Activity of Fe. Results reported here and previously[32,37,70] show that the intrinsic activity of FeOOH is much higher than previously thought and that the apparent activity of FeOOH is limited by its low conductivity. As discussed in the Introduction, Fe cations, then, are plausible active sites for OER. Therefore, understanding the activity of Fe in different local environments may help to better understand the range of highly active OER catalysts that utilize Fe.

Here, we compare the apparent TOFs across a number of Fe-containing samples including FeOOH/Au, FeOOH/Pt, Ni$_{0.75}$Fe$_{0.25}$OOH, and Co$_{0.54}$Fe$_{0.46}$OOH (Figure 6). We note

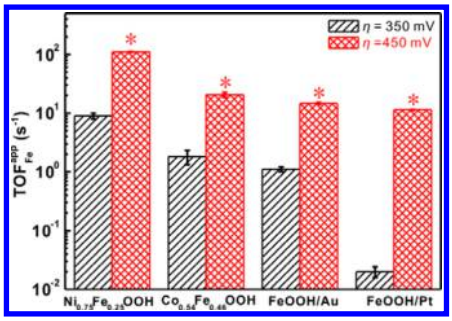

Figure 6. Intrinsic activity comparison based on the total film mass and composition assuming that only electrically accessible Fe-sites are available for catalysis during steady-state polarization at η = 350 and 450 mV. The asterisk (*) indicates that at η = 450 mV the current densities on those catalysts are large (~50−200 mA cm^{-2}) and could be potentially influenced by bubble/mass transport. As discussed in ref 37, the activity of the pure CoOOH and NiOOH phases is substantially lower than that of the Fe-containing phases, indicating that Fe is essential for the high activity.

that Fe-free NiOOH/Au and CoOOH/Au have much lower activities than the Fe-containing analogs, as has been discussed in detail in our previous publications.[37,70] For Ni$_{0.75}$Fe$_{0.25}$OOH and Co$_{0.54}$Fe$_{0.46}$OOH, the precise composition was chosen for roughly maximum TOF$_{tm}$[26,27,32,70] and determined by XPS. Here, however, apparent turnover frequencies are calculated assuming that only Fe-sites are available for catalysis (TOF$^{app}_{Fe}$). This is a different metric appropriate for comparing putative Fe site activity (compared to TOF$_{tm}$, which accounts for all metal cations and is more generally applicable). For the FeOOH/Au and FeOOH/Pt samples at η = 350 mV, we calculate TOF$^{app}_{Fe}$ assuming that only the first 0.1 μg cm^{-2} contributes to the OER

DOI: 10.1021/acs.chemmater.5b03404
Chem. Mater. 2015, 27, 8011−8020

activity (due to the electrical conductivity limitations discussed above). With these assumptions, we find that, at η = 350 mV, $Ni_{0.75}Fe_{0.25}OOH$ has the highest TOF_{Fe}^{app} of ca. 9 s^{-1}, higher than those of $Co_{0.54}Fe_{0.46}OOH$ (ca. 1.8 s^{-1}), FeOOH/Au (ca. 1.1 s^{-1}), and FeOOH/Pt (ca. 0.02 s^{-1}). Because $Ni_{0.75}Fe_{0.25}OOH$ and $Co_{0.54}Fe_{0.46}OOH$ are both highly conductive[15,32,37] and we have corrected (approximately) for the conductivity limitations of the FeOOH samples by counting only the first 0.1 $\mu g\ cm^{-2}$, these differences are presumably due to the intrinsic differences in the local structure of the active site(s).

At η = 450 mV, the TOF_{Fe}^{app} values of $Co_{0.54}Fe_{0.46}OOH$, FeOOH/Pt, and FeOOH/Au are similar (ca. 15 s^{-1}), whereas that of $Ni_{0.75}Fe_{0.25}OOH$ (ca. 110 s^{-1}) is larger. For the FeOOH/Au and FeOOH/Pt samples at η = 450 mV, we calculate TOF_{Fe}^{app} assuming that all of the Fe cations are possible actives sites as the film loading is small enough (<3 $\mu g\ cm^{-2}$) such that it is all electrically accessible at η = 450 mV. Friebel et al.[26] explained the high activity by Fe substituting for octahedral Ni with a Fe−O bond ∼6% shorter than that in γ-FeOOH. Correlating local structure to activity across the various Fe-containing phases would be important to further test this hypothesis.

3.7. Role of Au in Activating Interfacial FeOOH. A synergistic interaction between Au and iron oxide/hydroxide has been observed in many cases, including in CO oxidation,[71−73] the water−gas shift reaction,[74,75] and photocatalysis.[76] Generally, studies focus on how iron oxide/hydroxide improves the catalytic performance of Au. We reported that the presence of Fe impurities in alkaline electrolyte dramatically increases the OER activity of bare Au substrates.[15,32] This is intriguing as the OER activity of Au measured in $Ni(OH)_2$-cleaned Fe-free 1 M KOH is poor (Figure 4).[32] There are other indications that Fe activation of Au is important. Doyle and Lyons reported the cathodic superactivation of Au using a repetitive potential cycling procedure and found that the Tafel slope decreased from ca. 120 to ca. 48 mV dec^{-1} with increased activation of the Au surface.[77] The Tafel slope of the activated Au electrode (48 mV dec^{-1}) is similar to that of FeOOH/Au, and the repetitive potential cycling likely results in Fe incorporation. Karthik et al. used Fenton's reagent (i.e., Fe^{2+} + H_2O_2) to activate Au and observed that the overpotential for OER was lowered by 190 mV, consistent also with Fe surface contamination.[78] During the review of our work, Klaus et al. showed that Fe impurities deposited on oxidized Au electrodes serve as OER-active sites using density functional theory calculations.[79] In light of these findings, it is important to understand how Au interacts with Fe species and affects its OER catalytic performance.

Figure 7A shows a series of voltammetry cycles of a bare Au-QCM electrode in 1 M KOH that was not specifically cleaned for Fe impurities. The OER activity depends on the voltage sweep region. When sweeping from 0 to 0.7 V vs Hg/HgO, the OER activity increases with each cycle, as we have previously observed.[15,32] On the contrary, OER activity decreases with each cycle when sweeping only between 0.35 and 0.7 V. A similar decrease is also detected on the bare Pt QCM crystal, which has no clear redox features, even if the electrode is cycled from 0 to 0.7 V (Figure S9). Comparing the data, it appears that the difference lies in the presence/absence of Au redox features during activation. It is possible that the Au electrode could take up Fe impurities from electrolyte only during its oxidation/reduction. A bimetallic Au−Fe oxide/hydroxide at the electrode surface may be thus formed.

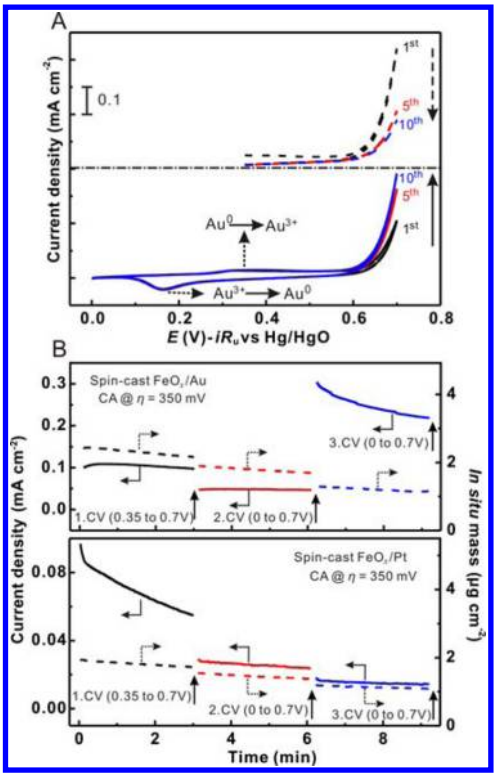

Figure 7. (A) Voltammetry on a bare Au QCM electrode in 1 M KOH solution from 0 to 0.7 V (bottom, solid lines) and 0.35 to 0.7 V (top, dash lines). (B) Chronoamperometry measurements on spin-cast FeO_x/Au (top) and FeO_x/Pt (bottom). At the indicated times, CVs were measured at a scan rate of 10 mV s^{-1} (see Figure S8).

We further tested spin-cast FeO_x films on Au. As shown in Figure 7B, the steady-state current density decreases after cycling between 0.35 and 0.7 V, which is probably due to the dissolution of FeO_x. A dramatic enhancement in activity is measured after cycling between 0 and 0.7 V. This data further supports the hypothesis that it is the oxidation/reduction of Au and the formation of the AuO_x that activates the FeOOH, perhaps through the formation of a hydrated Au−Fe mixed surface oxide. FeOOH simply in contact with the Au electrode does not appear to be sufficient to provide enhanced activity. Because AuO_x is electrically conductive,[80] this mixing would also lead to much better electronic coupling of Fe to the underlying metallic electrode. In the case of FeO_x/Pt, no such enhancement was observed, perhaps due to a smaller degree of Pt surface oxidation or to less optimal electronic interaction between the Pt and Fe cations. Further studies to directly identify Au−Fe mixed (and likely hydrated) oxides would be useful to confirm these hypotheses. This data is consistent with the experiments and density functional theory calculations by Klaus et al.[79]

4. CONCLUSIONS

We investigated the OER on FeOOH in alkaline media as a function of deposition method, film thickness (i.e., loading), and substrate type. At η = 350 mV, the electrical conductivity of FeOOH limits the number of Fe cations that can participate in OER, with only first ∼0.1 $\mu g\ cm^{-2}$ being sufficiently electrically integrated. These interfacial Fe cations are also influenced by the substrate, with the FeOOH on Au being substantially more

DOI: 10.1021/acs.chemmater.5b03404
Chem. Mater. 2015, 27, 8011−8020

active than on Pt. We found that the activation of FeOOH on Au depends on the electrode cycling history: Fe cations are activated for OER only when the Au substrate is cycled through the Au/AuO_x redox transition. At higher overpotentials (η = 450 mV), the electrical conductivity of FeOOH increases, more of the film (up to ~5 $\mu g\ cm^{-2}$) becomes OER active, and the geometric OER currents are similar on both Au and Pt. We also found that FeOOH films dissolved in 1 M KOH and that the dissolution rate was enhanced under anodic bias, suggesting the formation of soluble FeO_4^{2-}.

This work contributes to the growing body of evidence indicating that Fe is broadly important for OER catalysis under alkaline conditions.[37] Fe incorporation significantly increases the activity of NiOOH and CoOOH, and it has been proposed the Fe acts as the OER-active site (although the mechanism is still a matter of debate). The observations here that FeOOH itself is also highly active, albeit limited by electrical conductivity, and that Fe on Au/AuO_x has a similar per-Fe TOF as Co(Fe)OOH are consistent with this hypothesis. Leveraging new tools to study the role of Fe cations for OER in various chemical and electronic environments is likely to further improve our understanding of high-activity alkaline OER catalysts.

■ ASSOCIATED CONTENT

Supporting Information

The Supporting Information is available free of charge on the ACS Publications website at DOI: 10.1021/acs.chemmater.5b03404.

Additional diffraction, XPS and angle-resolved XPS, electron microscopy, voltammetry, and AC impedance data as well as details of TOF calculations (PDF)

■ AUTHOR INFORMATION

Corresponding Author

*E-mail: swb@uoregon.edu.

Notes

The authors declare no competing financial interest.

■ ACKNOWLEDGMENTS

This work was supported by the National Science Foundation (NSF) through a GOALI grant in partnership with Proton OnSite, CHE-1301461. S.Z. acknowledges financial support from the China Scholar Council. The authors thank Lisa Enman, Adam Smith, Adam Batchellor, and Athavan Nadarajah for insightful discussions. We acknowledge Stephen Golledge for help with XPS data interpretation. The project made use of CAMCOR facilities supported by grants from the W. M. Keck Foundation, the M. J. Murdock Charitable Trust, ONAMI, the Air Force Research Laboratory (FA86500515041), the National Science Foundation (0923577 and 0421086), and the University of Oregon. S.W.B. thanks the Research Corporation for Science Advancement, the Sloan Foundation, and the Camille and Henry Dreyfus Foundation for additional support.

■ REFERENCES

(1) Beni, G.; Schiavone, L. M.; Shay, J. L.; Dautremont-Smith, W. C.; Schneider, B. S. Electrocatalytic Oxygen Evolution on Reactively Sputtered Electrochromic Iridium Oxide Films. *Nature* **1979**, *282*, 281−283.

(2) Shimizu, Y.; Uemura, K.; Matsuda, H.; Miura, N.; Yamazoe, N. Bi-Functional Oxygen Electrode Using Large Surface Area $La_{1-x}Ca_xCoO_3$ for Rechargeable Metal-Air Battery. *J. Electrochem. Soc.* **1990**, *137*, 3430−3433.

(3) Lewis, N. S.; Nocera, D. G. Powering the Planet: Chemical Challenges in Solar Energy Utilization. *Proc. Natl. Acad. Sci. U. S. A.* **2006**, *103*, 15729−15735.

(4) Walter, M. G.; Warren, E. L.; McKone, J. R.; Boettcher, S. W.; Mi, Q.; Santori, E. A.; Lewis, N. S. Solar Water Splitting Cells. *Chem. Rev.* **2010**, *110*, 6446−6473.

(5) Trotochaud, L.; Mills, T. J.; Boettcher, S. W. An Optocatalytic Model for Semiconductor-Catalyst Water-Splitting Photoelectrodes Based on In Situ Optical Measurements on Operational Catalysts. *J. Phys. Chem. Lett.* **2013**, *4*, 931−935.

(6) Kanan, M. W.; Nocera, D. G. In Situ Formation of an Oxygen-Evolving Catalyst in Neutral Water Containing Phosphate and Co^{2+}. *Science* **2008**, *321*, 1072−1075.

(7) Suntivich, J.; May, K. J.; Gasteiger, H. A.; Goodenough, J. B.; Shao-Horn, Y. A Perovskite Oxide Optimized for Oxygen Evolution Catalysis from Molecular Orbital Principles. *Science* **2011**, *334*, 1383−1385.

(8) Liang, Y.; Li, Y.; Wang, H.; Zhou, J.; Wang, J.; Regier, T.; Dai, H. Co_3O_4 Nanocrystals on Graphene as a Synergistic Catalyst for Oxygen Reduction Reaction. *Nat. Mater.* **2011**, *10*, 780−786.

(9) Cobo, S.; Heidkamp, J.; Jacques, P.-A.; Fize, J.; Fourmond, V.; Guetaz, L.; Jousselme, B.; Ivanova, V.; Dau, H.; Palacin, S.; Fontecave, M.; Artero, V. A Janus Cobalt-Based Catalytic Material for Electro-Splitting of Water. *Nat. Mater.* **2012**, *11*, 802−807.

(10) Bediako, D. K.; Lassalle-Kaiser, B.; Surendranath, Y.; Yano, J.; Yachandra, V. K.; Nocera, D. G. Structure-Activity Correlations in a Nickel-Borate Oxygen Evolution Catalyst. *J. Am. Chem. Soc.* **2012**, *134*, 6801−6809.

(11) Doyle, R. L.; Godwin, I. J.; Brandon, M. P.; Lyons, M. E. G. Redox and Electrochemical Water Splitting Catalytic Properties of Hydrated Metal Oxide Modified Electrodes. *Phys. Chem. Chem. Phys.* **2013**, *15*, 13737−13783.

(12) Yamaguchi, A.; Inuzuka, R.; Takashima, T.; Hayashi, T.; Hashimoto, K.; Nakamura, R. Regulating Proton-Coupled Electron Transfer for Efficient Water Splitting by Manganese Oxides at Neutral PH. *Nat. Commun.* **2014**, *5*, 4256.

(13) Wu, Y.; Chen, M.; Han, Y.; Luo, H.; Su, X.; Zhang, M.-T.; Lin, X.; Sun, J.; Wang, L.; Deng, L.; Zhang, W.; Cao, R. Fast and Simple Preparation of Iron-Based Thin Films as Highly Efficient Water-Oxidation Catalysts in Neutral Aqueous Solution. *Angew. Chem., Int. Ed.* **2015**, *54*, 4870−4875.

(14) Trotochaud, L.; Ranney, J. K.; Williams, K. N.; Boettcher, S. W. Solution-Cast Metal Oxide Thin Film Electrocatalysts for Oxygen Evolution. *J. Am. Chem. Soc.* **2012**, *134*, 17253−17261.

(15) Trotochaud, L.; Young, S. L.; Ranney, J. K.; Boettcher, S. W. Nickel-Iron Oxyhydroxide Oxygen-Evolution Electrocatalysts: The Role of Intentional and Incidental Iron Incorporation. *J. Am. Chem. Soc.* **2014**, *136*, 6744−6753.

(16) Trotochaud, L.; Boettcher, S. W. Precise Oxygen Evolution Catalysts: Status and Opportunities. *Scr. Mater.* **2014**, *74*, 25−32.

(17) Chen, G.; Chen, L.; Ng, S.-M.; Man, W.-L.; Lau, T.-C. Chemical and Visible-Light-Driven Water Oxidation by Iron Complexes at pH 7−9: Evidence for Dual-Active Intermediates in Iron-Catalyzed Water Oxidation. *Angew. Chem., Int. Ed.* **2013**, *52*, 1789−1791.

(18) Nidola, A.; Trasatti, S. *Electrodes of Conductive Metallic Oxides*; Elsevier: Amsterdam, 1981.

(19) Trasatti, S. Electrocatalysis in the Anodic Evolution of Oxygen and Chlorine. *Electrochim. Acta* **1984**, *29*, 1503−1512.

(20) Lyons, M. E. G.; Brandon, M. P. The Oxygen Evolution Reaction on Passive Oxide Covered Transition Metal Electrodes in Alkaline Solution. Part III-Iron. *Int. J. Electrochem. Sci.* **2008**, *3*, 1463−1503.

(21) Subbaraman, R.; Tripkovic, D.; Chang, K.-C.; Strmcnik, D.; Paulikas, A. P.; Hirunsit, P.; Chan, M.; Greeley, J.; Stamenkovic, V.; Markovic, N. M. Trends in Activity for the Water Electrolyser Reactions on 3d M(Ni, Co, Fe, Mn) Hydr(oxy)oxide Catalysts. *Nat. Mater.* **2012**, *11*, 550−557.

DOI: 10.1021/acs.chemmater.5b03404
Chem. Mater. 2015, 27, 8011−8020

(22) Corrigan, D. A. The Catalysis of the Oxygen Evolution Reaction by Iron Impurities in Thin Film Nickel Oxide Electrodes. *J. Electrochem. Soc.* **1987**, *134*, 377−384.
(23) Louie, M. W.; Bell, A. T. An Investigation of Thin-Film Ni-Fe Oxide Catalysts for the Electrochemical Evolution of Oxygen. *J. Am. Chem. Soc.* **2013**, *135*, 12329−12337.
(24) Gong, M.; Li, Y.; Wang, H.; Liang, Y.; Wu, J. Z.; Zhou, J.; Wang, J.; Regier, T.; Wei, F.; Dai, H. An Advanced Ni-Fe Layered Double Hydroxide Electrocatalyst for Water Oxidation. *J. Am. Chem. Soc.* **2013**, *135*, 8452−8455.
(25) Smith, A. M.; Trotochaud, L.; Burke, M. S.; Boettcher, S. W. Contributions to Activity Enhancement via Fe Incorporation in Ni-(Oxy)hydroxide/Borate Catalysts for Near-Neutral pH Oxygen Evolution. *Chem. Commun.* **2015**, *51*, 5261−5263.
(26) Friebel, D.; Louie, M. W.; Bajdich, M.; Sanwald, K. E.; Cai, Y.; Wise, A. M.; Cheng, M.-J.; Sokaras, D.; Weng, T.-C.; Alonso-Mori, R.; Davis, R. C.; Bargar, J. R.; Nørskov, J. K.; Nilsson, A.; Bell, A. T. Identification of Highly Active Fe Sites in (Ni,Fe)OOH for Electrocatalytic Water Splitting. *J. Am. Chem. Soc.* **2015**, *137*, 1305−1313.
(27) Klaus, S.; Cai, Y.; Louie, M. W.; Trotochaud, L.; Bell, A. T. Effects of Fe Electrolyte Impurities on $Ni(OH)_2$/NiOOH Structure and Oxygen Evolution Activity. *J. Phys. Chem. C* **2015**, *119*, 7243−7254.
(28) Gong, M.; Dai, H. A Mini Review of NiFe-Based Materials as Highly Active Oxygen Evolution Reaction Electrocatalysts. *Nano Res.* **2015**, *8*, 23−39.
(29) Iwakura, C.; Honji, A.; Tamura, H. The Anodic Evolution of Oxygen on Co_3O_4 Film Electrodes in Alkaline Solutions. *Electrochim. Acta* **1981**, *26*, 1319−1326.
(30) Xiao, C.; Lu, X.; Zhao, C. Unusual Synergistic Effects upon Incorporation of Fe and/or Ni into Mesoporous Co_3O_4 for Enhanced Oxygen Evolution. *Chem. Commun.* **2014**, *50*, 10122−10125.
(31) Grewe, T.; Deng, X.; Tüysüz, H. Influence of Fe Doping on Structure and Water Oxidation Activity of Nanocast Co_3O_4. *Chem. Mater.* **2014**, *26*, 3162−3168.
(32) Burke, M. S.; Kast, M. G.; Trotochaud, L.; Smith, A. M.; Boettcher, S. W. Cobalt−Iron (Oxy)hydroxide Oxygen Evolution Electrocatalysts: The Role of Structure and Composition on Activity, Stability, and Mechanism. *J. Am. Chem. Soc.* **2015**, *137*, 3638−3648.
(33) Burke, L. D.; Lyons, M. E. G. The Formation and Stability of Hydrous Oxide Films on Iron under Potential Cycling Conditions in Aqueous Solution at High pH. *J. Electroanal. Chem. Interfacial Electrochem.* **1986**, *198*, 347−368.
(34) Lyons, M. E. G.; Brandon, M. P. A Comparative Study of the Oxygen Evolution Reaction on Oxidised Nickel, Cobalt and Iron Electrodes in Base. *J. Electroanal. Chem.* **2010**, *641*, 119−130.
(35) Lyons, M. E. G.; Brandon, M. P. Redox Switching and Oxygen Evolution Electrocatalysis in Polymeric Iron Oxyhydroxide Films. *Phys. Chem. Chem. Phys.* **2009**, *11*, 2203−2217.
(36) Lyons, M. E. G.; Doyle, R. L.; Brandon, M. P. Redox Switching and Oxygen Evolution at Oxidized Metal and Metal Oxide Electrodes: Iron in Base. *Phys. Chem. Chem. Phys.* **2011**, *13*, 21530−21551.
(37) Burke, M. S.; Zou, S.; Enman, L. J.; Kellon, J. E.; Gabor, C. A.; Pledger, E.; Boettcher, S. W. Revised Oxygen Evolution Reaction Activity Trends for First-Row Transition-Metal (Oxy)hydroxides in Alkaline Media. *J. Phys. Chem. Lett.* **2015**, *6*, 3737−3742.
(38) Rüetschi, P.; Delahay, P. Influence of Electrode Material on Oxygen Overvoltage: A Theoretical Analysis. *J. Chem. Phys.* **1955**, *23*, 556−560.
(39) Bockris, J. O. M.; Otagawa, T. The Electrocatalysis of Oxygen Evolution on Perovskites. *J. Electrochem. Soc.* **1984**, *131*, 290−302.
(40) Bockris, J. O.; Otagawa, T. Mechanism of Oxygen Evolution on Perovskites. *J. Phys. Chem.* **1983**, *87*, 2960−2971.
(41) Calle-Vallejo, F.; Díaz-Morales, O. A.; Kolb, M. J.; Koper, M. T. M. Why Is Bulk Thermochemistry a Good Descriptor for the Electrocatalytic Activity of Transition Metal Oxides? *ACS Catal.* **2015**, *5*, 869−873.
(42) Man, I. C.; Su, H.-Y.; Calle-Vallejo, F.; Hansen, H. A.; Martínez, J. I.; Inoglu, N. G.; Kitchin, J.; Jaramillo, T. F.; Nørskov, J. K.; Rossmeisl, J. Universality in Oxygen Evolution Electrocatalysis on Oxide Surfaces. *ChemCatChem* **2011**, *3*, 1159−1165.
(43) Cornell, R. M.; Schwertmann, U. *The Iron Oxides: Structure, Properties, Reactions, Occurrences and Uses*; John Wiley & Sons: Weinheim, Germany, 2006.
(44) Chen, C. T.; Cahan, B. D. The Nature of the Passive Film on Iron: I. Automatic Ellipsometric Spectroscopy Studies. *J. Electrochem. Soc.* **1982**, *129*, 17−26.
(45) Cahan, B. D.; Chen, C. T. The Nature of the Passive Film on Iron: II. A-C Impedance Studies. *J. Electrochem. Soc.* **1982**, *129*, 474−480.
(46) Sauerbrey, G. Verwendung von Schwingquarzen zur Wägung dünner Schichten und zur Mikrowägung. *Eur. Phys. J. A* **1959**, *155*, 206−222.
(47) Fadley, C. S. Surface Analysis, Peak Intensities and Angular Distributions in XPS. *Faraday Discuss. Chem. Soc.* **1975**, *60*, 18−29.
(48) Chemelewski, W. D.; Lee, H.-C.; Lin, J.-F.; Bard, A. J.; Mullins, C. B. Amorphous FeOOH Oxygen Evolution Reaction Catalyst for Photoelectrochemical Water Splitting. *J. Am. Chem. Soc.* **2014**, *136*, 2843−2850.
(49) Martinez, L.; Leinen, D.; Martín, F.; Gabas, M.; Ramos-Barrado, J. R.; Quagliata, E.; Dalchiele, E. A. Electrochemical Growth of Diverse Iron Oxide (Fe_3O_4, α-FeOOH, and γ-FeOOH) Thin Films by Electrodeposition Potential Tuning. *J. Electrochem. Soc.* **2007**, *154*, 126−133.
(50) Smith, R. D. L.; Prévot, M. S.; Fagan, R. D.; Zhang, Z.; Sedach, P. A.; Siu, M. K. J.; Trudel, S.; Berlinguette, C. P. Photochemical Route for Accessing Amorphous Metal Oxide Materials for Water Oxidation Catalysis. *Science* **2013**, *340*, 60−63.
(51) Seabold, J. A.; Choi, K.-S. Efficient and Stable Photo-Oxidation of Water by a Bismuth Vanadate Photoanode Coupled with an Iron Oxyhydroxide Oxygen Evolution Catalyst. *J. Am. Chem. Soc.* **2012**, *134*, 2186−2192.
(52) Kurzman, J. A.; Dettelbach, K. E.; Martinolich, A. J.; Berlinguette, C. P.; Neilson, J. R. Structural Characteristics and Eutaxy in the Photo-Deposited Amorphous Iron Oxide Oxygen Evolution Catalyst. *Chem. Mater.* **2015**, *27*, 3462−3470.
(53) Schweitzer, G. K.; Pesterfield, L. L. *The Aqueous Chemistry of the Elements*; Oxford University Press: Oxford, 2010.
(54) Bernal, J.; Dasgupta, D.; Mackay, A. The Oxides and Hydroxides of Iron and Their Structural Inter-Relationships. *Clay Miner.* **1959**, *4*, 15−30.
(55) Yang, J.; Liu, H.; Martens, W. N.; Frost, R. L. Synthesis and Characterization of Cobalt Hydroxide, Cobalt Oxyhydroxide, and Cobalt Oxide Nanodiscs. *J. Phys. Chem. C* **2010**, *114*, 111−119.
(56) Zou, G.; Liu, R.; Chen, W. Highly Textural Lamellar Mesostructured Magnesium Hydroxide via a Cathodic Electrodeposition Process. *Mater. Lett.* **2007**, *61*, 1990−1993.
(57) Guo, X.; Zhang, F.; Evans, D. G.; Duan, X. Layered Double Hydroxide Films: Synthesis, Properties and Applications. *Chem. Commun.* **2010**, *46*, 5197−5210.
(58) Chang, S. H.; Connell, J. G.; Danilovic, N.; Subbaraman, R.; Chang, K.-C.; Stamenkovic, V. R.; Markovic, N. M. Activity-Stability Relationship in the Surface Electrochemistry of the Oxygen Evolution Reaction. *Faraday Discuss.* **2014**, *176*, 125−133.
(59) Frydendal, R.; Paoli, E. A.; Knudsen, B. P.; Wickman, B.; Malacrida, P.; Stephens, I. E. L.; Chorkendorff, I. Benchmarking the Stability of Oxygen Evolution Reaction Catalysts: The Importance of Monitoring Mass Losses. *ChemElectroChem* **2014**, *1*, 2075−2081.
(60) Danilovic, N.; Subbaraman, R.; Chang, K.-C.; Chang, S. H.; Kang, Y. J.; Snyder, J.; Paulikas, A. P.; Strmcnik, D.; Kim, Y.-T.; Myers, D.; Stamenkovic, V. R.; Markovic, N. M. Activity−Stability Trends for the Oxygen Evolution Reaction on Monometallic Oxides in Acidic Environments. *J. Phys. Chem. Lett.* **2014**, *5*, 2474−2478.
(61) Frydendal, R.; Busch, M.; Halck, N. B.; Paoli, E. A.; Krtil, P.; Chorkendorff, I.; Rossmeisl, J. Enhancing Activity for the Oxygen

DOI: 10.1021/acs.chemmater.5b03404
Chem. Mater. 2015, 27, 8011−8020

Evolution Reaction: The Beneficial Interaction of Gold with Manganese and Cobalt Oxides. *ChemCatChem* **2015**, *7*, 149−154.
(62) Gorlin, Y.; Chung, C.-J.; Benck, J. D.; Nordlund, D.; Seitz, L.; Weng, T.-C.; Sokaras, D.; Clemens, B. M.; Jaramillo, T. F. Understanding Interactions between Manganese Oxide and Gold That Lead to Enhanced Activity for Electrocatalytic Water Oxidation. *J. Am. Chem. Soc.* **2014**, *136*, 4920−4926.
(63) Yeo, B. S.; Bell, A. T. Enhanced Activity of Gold-Supported Cobalt Oxide for the Electrochemical Evolution of Oxygen. *J. Am. Chem. Soc.* **2011**, *133*, 5587−5593.
(64) Yeo, B. S.; Bell, A. T. In Situ Raman Study of Nickel Oxide and Gold-Supported Nickel Oxide Catalysts for the Electrochemical Evolution of Oxygen. *J. Phys. Chem. C* **2012**, *116*, 8394−8400.
(65) Lu, X.; Ng, Y. H.; Zhao, C. Gold Nanoparticles Embedded within Mesoporous Cobalt Oxide Enhance Electrochemical Oxygen Evolution. *ChemSusChem* **2014**, *7*, 82−86.
(66) Chang, S. H.; Danilovic, N.; Chang, K.-C.; Subbaraman, R.; Paulikas, A. P.; Fong, D. D.; Highland, M. J.; Baldo, P. M.; Stamenkovic, V. R.; Freeland, J. W.; Eastman, J. A.; Markovic, N. M. Functional Links between Stability and Reactivity of Strontium Ruthenate Single Crystals during Oxygen Evolution. *Nat. Commun.* **2014**, *5*, 4191.
(67) Viswanathan, V.; Pickrahn, K. L.; Luntz, A. C.; Bent, S. F.; Nørskov, J. K. Nanoscale Limitations in Metal Oxide Electrocatalysts for Oxygen Evolution. *Nano Lett.* **2014**, *14*, 5853−5857.
(68) Trasatti, S. Physical Electrochemistry of Ceramic Oxides. *Electrochim. Acta* **1991**, *36*, 225−241.
(69) Lin, F.; Bachman, B. F.; Boettcher, S. W. Impact of Electrocatalyst Activity and Ion Permeability on Water-Splitting Photoanodes. *J. Phys. Chem. Lett.* **2015**, *6*, 2427−2433.
(70) Burke, M. S.; Enman, L. J.; Batchellor, A. S.; Zou, S.; Boettcher, S. W. Oxygen-Evolution-Reaction Electrocatalysis on Transition Metal Oxides and (Oxy)hydroxides: Activity Trends and Design Principles. *Chem. Mater.* **2015**, DOI: 10.1021/acs.chemmater.5b03148.
(71) Bond, G.; Thompson, D. Gold-Catalysed Oxidation of Carbon Monoxide. *Gold Bull.* **2000**, *33*, 41−50.
(72) Finch, R. M.; Hodge, N. A.; Hutchings, G. J.; Meagher, A.; Pankhurst, Q. A.; Siddiqui, M. R. H.; Wagner, F. E.; Whyman, R. Identification of Active Phases in Au-Fe Catalysts for Low-Temperature CO Oxidation. *Phys. Chem. Chem. Phys.* **1999**, *1*, 485−489.
(73) Hao, Z.; An, L.; Wang, H.; Hu, T. Mechanism of Gold Activation in Supported Gold Catalysts for CO Oxidation. *React. Kinet. Catal. Lett.* **2000**, *70*, 153−160.
(74) Andreeva, D.; Idakiev, V.; Tabakova, T.; Andreev, A. Low-Temperature Water-Gas Shift Reaction over Au/α-Fe_2O_3. *J. Catal.* **1996**, *158*, 354−355.
(75) Andreeva, D.; Idakiev, V.; Tabakova, T.; Andreev, A.; Giovanoli, R. Low-Temperature Water-Gas Shift Reaction on Au/α-Fe_2O_3 Catalyst. *Appl. Catal., A* **1996**, *134*, 275−283.
(76) Wu, Y.; Zhang, J.; Xiao, L.; Chen, F. Preparation and Characterization of TiO_2 Photocatalysts by Fe^{3+} Doping Together with Au Deposition for the Degradation of Organic Pollutants. *Appl. Catal., B* **2009**, *88*, 525−532.
(77) Doyle, R.; Lyons, M. G. The Mechanism of Oxygen Evolution at Superactivated Gold Electrodes in Aqueous Alkaline Solution. *J. Solid State Electrochem.* **2014**, *18*, 3271−3286.
(78) Karthik, P. E.; Jeyabharathi, C.; Phani, K. L. Oxygen Evolution Reaction Electrocatalyzed on a Fenton-Treated Gold Surface. *Chem. Commun.* **2014**, *50*, 2787−2790.
(79) Klaus, S.; Trotochaud, L.; Cheng, M.-J.; Head-Gordon, M.; Bell, A. T. Experimental and Computational Evidence of Highly Active Fe Impurity Sites on the Surface of Oxidized Au for the Electrocatalytic Oxidation of Water in Basic Media. *ChemElectroChem* **2015**, DOI: 10.1002/celc.201500364.
(80) Machalett, F.; Edinger, K.; Melngailis, J.; Diegel, M.; Steenbeck, K.; Steinbeiss, E. Direct Patterning of Gold Oxide Thin Films by Focused Ion-Beam Irradiation. *Appl. Phys. A: Mater. Sci. Process.* **2000**, *71*, 331−335.

DOI: 10.1021/acs.chemmater.5b03404
Chem. Mater. 2015, 27, 8011−8020